# Mitigation of the internal *p-n* junction in $CoS_2$-contacted $FeS_2$ single crystals: Accessing bulk semiconducting transport

Bryan Voigt,[1] Bhaskar Das,[1] David M. Carr,[2] Debmalya Ray,[3] Moumita Maiti,[1] William Moore,[1] Michael Manno,[1] Jeff Walter,[1,4] Eray S. Aydil,[5,*] and Chris Leighton[1,†]

[1]*Department of Chemical Engineering and Materials Science, University of Minnesota, Minneapolis, Minnesota 55455, USA*

[2]*Physical Electronics, Inc., Chanhassen, Minnesota 55317, USA*

[3]*Department of Chemistry, University of Minnesota, Minneapolis, Minnesota 55455, USA*

[4]*Department of Physics, Augsburg University, Minneapolis, Minnesota 55454, USA*

[5]*Department of Chemical and Biomolecular Engineering, New York University Tandon School of Engineering, Brooklyn, New York 11201, USA*

(Received 23 December 2020; accepted 15 February 2021; published 26 February 2021)

Pyrite $FeS_2$ is an outstanding candidate for a low-cost, nontoxic, sustainable photovoltaic material, but efficient pyrite-based solar cells are yet to materialize. Recent studies of single crystals have shed much light on this by uncovering a *p*-type surface inversion layer on *n*-type (S-vacancy doped) crystals, and the resulting internal *p-n* junction. This leaky internal junction likely plays a key role in limiting efficiency in pyrite-based photovoltaic devices, also obscuring the true bulk semiconducting transport properties of pyrite crystals. Here, we demonstrate complete mitigation of the internal *p-n* junction in $FeS_2$ crystals by fabricating metallic $CoS_2$ contacts via a process that simultaneously diffuses Co (a shallow donor) into the crystal, the resulting heavy *n* doping yielding direct Ohmic contact to the interior. Low-temperature bulk transport studies of controllably Co- and S-vacancy doped semiconducting crystals then enable a host of previously inaccessible observations and measurements, including determination of donor activation energies (which are as low as 5 meV for Co), observation of an unexpected second activated transport regime, realization of electron mobility up to 2100 $cm^2\ V^{-1}\ s^{-1}$, elucidation of very different mobilities in Co- and S-vacancy-doped cases, and observation of an abrupt temperature-dependent crossover to bulk Efros-Shklovskii variable-range hopping, accompanied by an unusual form of nonlinear Hall effect. Aspects of the results are interpreted with the aid of first-principles electronic structure calculations on both Co- and S-vacancy-doped $FeS_2$. This work thus demonstrates unequivocal mitigation of the internal *p-n* junction in pyrite single crystals, with important implications for both future fundamental studies and photovoltaic devices.

DOI: 10.1103/PhysRevMaterials.5.025405

## I. INTRODUCTION

Due to outstanding visible light absorption, adequate electron mobility and minority carrier diffusion length, exceptionally low cost [1], and earth-abundant nontoxic constituents [1], pyrite-structure $FeS_2$ has long been considered an attractive sustainable photovoltaic material [2]. Pyrite-based heterojunction solar cells have disappointing power conversion efficiencies, however (typically <3%), limited by low open-circuit voltages ($V_{OC}$), even in single-crystal devices [2–7]. While historically a matter of debate [2–7], recent work provides compelling evidence that the low $V_{OC}$ originates in a leaky *p-n* junction *internal* to pyrite [7–10]. Specifically, several recent publications on high-quality single crystals report a nanometer (nm)-thick *p*-type inversion layer on the surface of unintentionally *n*-doped pyrite [8,9,11], leading to the situation shown schematically in Fig. 1(a). Consistent with earlier observations of surface-state-driven pinning of the Fermi level near the valence band maximum [2,12–14], substantial near-surface band bending is thought to occur [Fig. 1(a)]. In horizontal single-crystal transport measurements, conspicuous surface conduction then arises, the electrical resistivity ($\rho$) abruptly flattening on cooling as bulk carrier freeze-out leads to current shunting by the heavily *p*-doped surface [9,11]. Such behavior has been quantitatively captured by two-channel (bulk and surface) modeling [9,11]. Strong evidence has also been accumulated that S-vacancy ($V_S$)-based native defects are present [2,14,15] and responsible for the unintentional bulk *n* doping in such crystals [as in Fig. 1(a)] [16,17]. Experiments have identified a ~225 meV deep donor and linked it to $V_S$ [16], while computational work implicates $V_S$ *clusters* as the likely donors [17].

Most recently, $\rho(T)$ measurements on single crystals with systematically-controlled S vacancy concentration ($[V_S]$) directly revealed the internal junction between the *n*-type interior and *p*-type surface [10] [i.e., the depletion region in Fig. 1(a)]. At sufficiently high $[V_S]$ (i.e., low bulk resistance), the exponential $T$ dependence of the internal *p-n* junction resistance was shown to abruptly cut off current to the crystal interior on cooling, leading to an abrupt $10^4$-fold increase in

*aydil@nyu.edu
†leighton@umn.edu

 

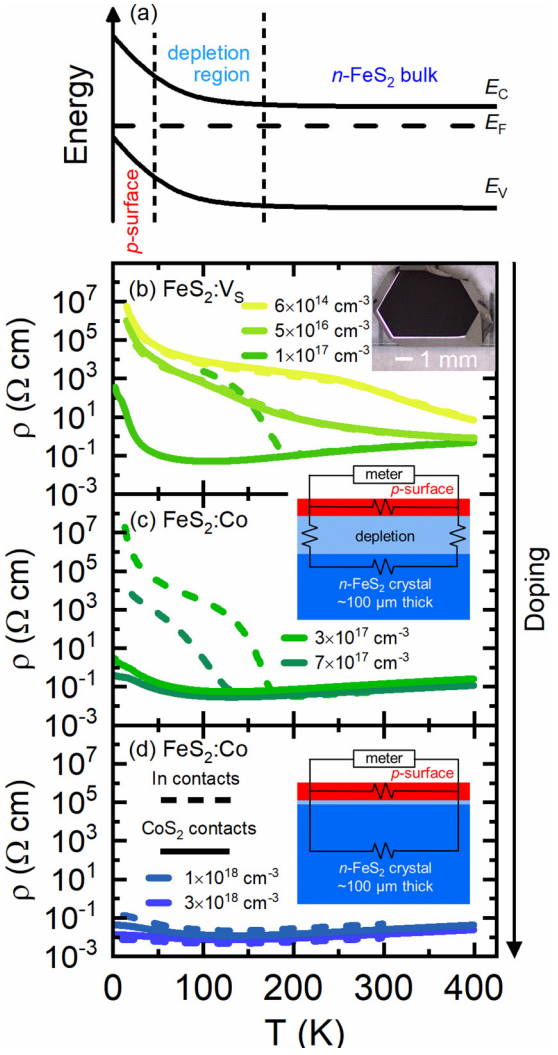


FIG. 1. (a) Schematic band diagram of an $n$-$FeS_2$ crystal (with the surface on the extreme left). Shown are the conduction band ($E_C$), valence band ($E_V$), and Fermi ($E_F$) energies, along with the $n$-bulk, $p$-$n$ depletion, and $p$-surface regions. Note the substantial upward band bending toward the surface. For scale, the accepted energy gap in $FeS_2$ is ∼0.95 eV. Temperature ($T$) dependence of the resistivity ($\rho$) of $FeS_2$ single crystals with (b) light S vacancy ($V_S$) doping [$n(300\,\mathrm{K}) = 6 \times 10^{14},\ 5 \times 10^{15},\ 1 \times 10^{17}\,\mathrm{cm}^{-3}$], (c) moderate Co doping [$n(300\,\mathrm{K}) = 3 \times 10^{17}, 7 \times 10^{17}\,\mathrm{cm}^{-3}$], and (d) heavy Co doping [$n(300\,\mathrm{K}) = 1 \times 10^{18},\ 3 \times 10^{18}\,\mathrm{cm}^{-3}$]. [$n$(300 K) is the 300 K Hall electron density]. Data are shown for both In contacts (dashed lines) and $CoS_2$ contacts (solid lines). A typical crystal is shown in (b) (adapted with permission from Ref. [16]. Copyright 2019 American Chemical Society). The insets to (c), (d) are schematics (not to scale) showing the $n$-type bulk (dark blue), $p$-type surface (red), $p$-$n$ depletion region (light blue), and equivalent circuit diagrams. Note that due to heavy doping in the $p$-type surface layer, the depletion width is controlled by the $n$ doping in the crystal interior.

$\rho$ at ∼130–200 K [10]. Three-channel [bulk, surface, junction (depletion region)] modeling describing the internal $p$-$n$ interface as a Schottky junction was shown to quantitatively reproduce the [$V_S$]-dependent $\rho(T)$, enabling extraction of junction barrier heights [10]. The latter exhibit significant variance even in nominally identical crystals, averaging to ∼320 meV [10]. Given this low average barrier height (notably close to $V_{OC}$ in pyrite crystal based heterojunction solar cells [2–7]), the distribution in barrier heights (consistent with the variability in such cells [2–7]), and the substantial voltage deficit relative to simple band bending expectations [⩾750 meV; see Fig. 1(a)] [10], it was concluded that a leaky internal $p$-$n$ junction plays a key role in limiting $V_{OC}$, and thus efficiency, in pyrite-based heterojunction photovoltaic devices [10]. In essence, devices such as prior metal/$FeS_2$ Schottky cells [6] were in reality likely metal/heavily $p$-doped $FeS_2$ surface/internal junction/bulk $n$-type $FeS_2$ heterostructures, the $V_{OC}$ deriving largely from the internal $p$-$n$ junction.

An important consequence of the above is that the bulk electronic transport properties of semiconducting pyrite $FeS_2$ single crystals have been inaccessible below ∼200 K, due to obfuscation by the internal junction. With no cryogenic measurements of the $T$-dependent bulk $\rho$, Hall electron density, and Hall mobility, for example, essential characterization of the electronic transport mechanisms in pyrite remains lacking. Just some of the gaps in fundamental understanding include the interplay between bulk diffusive and hopping transport and the general level of disorder in state of the art $FeS_2$ crystals; accurate positions of the donor levels for known $n$-type pyrite dopants; the behavior of mobility vs $T$ and doping level for different donors, and thus the overall electronic quality in comparison to semiconductors such as Si; the relative importance of scattering from phonons, ionized impurities, and other defects; the nature of the approach to the insulator-metal transition (IMT) (which is of particular interest for deep donors such as $V_S$ [16]); and the possibility of quantum transport (e.g., Shubnikov–de Haas oscillations) in crystals doped beyond the IMT, which could elucidate additional important transport parameters. Such information is important not only fundamentally but also for applications, such as in photovoltaics. Sufficiently advanced understanding of doping, for example, could enable mitigation of $V_S$ deep donor concentrations to improve $V_{OC}$ [7,9]; identification of ideal $n$ dopants for future pyrite PV devices; and identification and characterization of workable $p$ dopants, and thus the development of future *homojunction* $FeS_2$ solar cells, which could sidestep issues with surface states. A means to mitigate the internal $p$-$n$ junction in pyrite single crystals, thereby enabling bulk transport characterization, is thus highly desirable.

We address this challenge here by demonstrating that appropriately fabricated $CoS_2$ thin film overlayers on $FeS_2$ bulk single crystals enable direct Ohmic contact to the crystal interior. $CoS_2$ has the same pyrite structure as $FeS_2$ but $t_{2g}{}^6e_g^1$ electronic configuration (cf. $t_{2g}{}^6e_g^0$ in $FeS_2$), resulting in metallicity and ferromagnetism with a Curie temperature $T_C \approx 120$ K [18,19]. We form $CoS_2$ by *ex situ* sulfidation of Co films at elevated temperature in a S atmosphere [20], simultaneously inducing reaction of the Co film to $CoS_2$ and significant interdiffusion of Co into the $FeS_2$ crystal, as verified by time of flight secondary ion mass spectrometry (TOF SIMS) depth profiling. As $CoS_2$ is metallic [19,20] and Co is a shallow donor in $FeS_2$ [10,21–24], this results in a metallic contact on an $FeS_2$ surface where heavy doping under the $CoS_2$ yields direct Ohmic contact to the crystal interior (through mechanisms we elucidate). Transport measurements on semiconducting $V_S$- and Co-doped crystals

then demonstrate complete mitigation of the internal junction, providing direct access to bulk electronic properties. We thereby report a host of quantities and phenomena, including donor activation energies (down to 5 meV for Co), an unexpected second activated transport regime, electron mobility to 2100 $cm^2\ V^{-1}\ s^{-1}$, elucidation of very different mobilities in Co- and $V_S$-doped cases, and an abrupt $T$-dependent crossover to bulk Efros-Shklovskii variable-range hopping (ES VRH) [25] accompanied by an unusual nonlinear Hall effect. Aspects of the results are interpreted via first-principles electronic structure calculations. Unequivocal mitigation of the internal *p-n* junction in pyrite single crystals is thus demonstrated, with implications for future fundamental studies and pyrite photovoltaic devices.

## II. EXPERIMENTAL AND COMPUTATIONAL DETAILS

As discussed previously [10,11,16,26–28] and summarized in the Supplemental Material, Sec. A [29], high-quality pyrite single crystals [Fig. 1(b), inset] were grown by chemical vapor transport. Controlled doping with $V_S$ or Co was achieved by S vapor pressure tuning during growth [10,16] and direct Co incorporation [10], respectively. The resulting crystals have been extensively characterized via powder x-ray diffraction, high-resolution single-crystal x-ray diffraction, x-ray rocking curves, energy dispersive x-ray spectroscopy, particle-induced x-ray emission, mass spectrometry, Raman spectroscopy, and atomic force microscopy [10,11,16,26–28]. Phase-pure, uniform, low defect density, low impurity concentration ($\leqslant$40 ppm metals basis; see Ref. [16]) crystals have been thus established [10,11,16,26–28].

Electronic transport measurement details are provided in the Supplemental Material (Sec. B) [29]. Briefly, polished crystals [11] were used for all measurements, employing soldered In as a standard contact [10,16]. Alternatively, for $CoS_2$ contacts, ~30 nm thick Co films were sputtered or evaporated on crystal surfaces (forming contact pads), then *ex situ* sulfidized for 8 h at 350 °C in an ~8 $cm^3$ quartz ampoule with 5 mg of S. As expected [20], this yields phase-pure metallic ferromagnetic $CoS_2$, with a volume expansion factor of ~3.85 (i.e., $CoS_2$ thickness ~120 nm). X-ray diffraction (XRD) characterization of $CoS_2$ contact films was done on a Bruker D8 Discover diffractometer with a two-dimensional (2D) detector, magnetic characterization was performed in a Quantum Design MPMS, and TOF SIMS characterization of the $CoS_2/FeS_2$ interface was done in a PHI *nano*TOF II. Silver paint was used to contact the $CoS_2$ thin film pads; then four-wire van der Pauw measurements were made in DC and AC (16 Hz) modes, from 1.8 to 400 K in magnetic flux densities ($B$) up to 9 T.

As detailed in the Supplemental Material [29], density functional theory (DFT) calculations were also performed to aid in the interpretation of some of the experimental results. These used the Vienna *ab initio* simulation package (VASP) [30–33], employing projected augmented wave pseudopotentials [34,35] and Perdew-Burke-Ernzerhof exchange-correlation functionals [36,37] with a Hubbard $U$ correction [38]. All details, including the choice of $U$ (for Fe and Co), are described in the Supplemental Material [29]. Co- and $V_S$-doped $FeS_2$ were modeled in a $3 \times 3 \times 3$ supercell containing one $Co_{Fe}$ or a tetra-S-vacancy defect. The latter was found in recent work [17] to correspond most closely to experimental observations, highlighting the likely role of $V_S$ clusters.

## III. RESULTS AND DISCUSSION

Shown first in Figs. 1(b)–1(d) are $\rho(T)$ data from crystals doped lightly with $V_S$ [Fig. 1(b)], moderately with Co [Fig. 1(c)], and heavily with Co [Fig. 1(d)], i.e., with increasing doping from top to bottom. Respective (300 K) Hall electron densities [$n$(300 K)] are shown in each case, along with data taken with both In (dashed lines) and $CoS_2$ (solid lines) contacts. Starting at $n(300\,K) = 6 \times 10^{14}\ cm^{-3}$ [yellow, Fig. 1(b)], typical lightly doped single-crystal $FeS_2$ behavior is observed [9–11,16], $\rho(T)$ first increasing upon cooling, then flattening at ~250 K, before rising again below ~50 K. As discussed above, this reflects freeze-out of the $n$-type interior as $T$ is reduced from room temperature, followed by shunting by the more conductive heavily $p$-doped surface layer [see Fig. 1(a)] at low $T$ [9–11,16]. (Thickness scaling, among other observations, confirmed low $T$ surface conduction in prior work [9–11,16].) Increasing $V_S$ doping to $n(300\,K) = 5 \times 10^{16}\ cm^{-3}$ yields similar behavior, but with a bulk to surface conduction crossover at lower $T$ (~100 K) due to lower bulk resistance. Significantly, in both of these cases the dashed and solid lines (In and $CoS_2$ contacts) are indistinguishable; low $T$ current shunting by the exposed crystal surface between the contacts occurs regardless of the contact material. In the heaviest $V_S$-doped crystal in Fig. 1(b), however [$n(300\,K) = 1 \times 10^{17}\ cm^{-3}$], In and $CoS_2$ contacts generate strikingly different $\rho(T)$ at low $T$. [$V_S$] is now high enough to induce metalliclike, phonon-limited bulk $\rho(T)$ at high $T$ (i.e., $d\rho/dT > 0$), but, consistent with our recent report [10] and the above Introduction, $\rho(T)$ with In contacts shows an abrupt $10^4$-fold increase below ~200 K. This reflects the equivalent circuit in the inset to Fig. 1(c), where the exponential rise of the *p-n* depletion region resistance on cooling (dictated by the ~300 meV junction barrier height) abruptly cuts off current to the crystal interior, restricting conduction to the surface layer only [10].

The $n(300\,K) = 1 \times 10^{17}\ cm^{-3}\ \rho(T)$ measured instead with $CoS_2$ contacts [Fig. 1(b), lowest solid line] provides a central result of this work. In stark contrast to the In contact case, no abrupt sub-200 K rise in $\rho(T)$ occurs, $\rho$ being up to $10^4$ times lower than with In. The resistivity instead gradually decreases down to ~100 K before rising to ~$10^3\ \Omega\,cm$ at 1.8 K. All characteristic $\rho(T)$ signatures of the internal *p-n* junction depletion region are thus *entirely eliminated* with *ex situ* sulfidized $CoS_2$ contacts, suggesting *direct contact to the crystal interior*. This is indicated not only by the absence of the abrupt rise in $\rho(T)$ below ~200 K, but also by the very low magnitude of the low $T$ resistivity and resistance, far beneath anything associated with 2D surface conduction in $FeS_2$ crystals. These conclusions are further reinforced below by essentially all of the performed transport measurements. Figure 1(c) shows that such behavior also occurs in moderately Co-doped crystals, the abrupt 125–175 K increase in $\rho(T)$ with In contacts being entirely extinguished with $CoS_2$ contacts. The increased doping here [up to $n(300\,K) = 7 \times 10^{17}\ cm^{-3}$] leads to quite weak $\rho(T)$ in $CoS_2$-contacted

crystals, $\rho(T \to 0)$ in fact becoming finite. (A detailed study of the IMT with Co doping will be presented elsewhere [39]). The situation then changes at heavy Co doping [up to $n(300\,\mathrm{K}) = 3 \times 10^{18}\,\mathrm{cm}^{-3}$, Fig. 1(d)], where near $T$-independent resistivity occurs, approaching 1 m$\Omega$ cm. In this clearly metallic regime, $\rho(T)$ measured with In and $CoS_2$ contacts becomes essentially indistinguishable, again consistent with the equivalent circuit in the inset to Fig. 1(d). The $n$ doping is sufficiently high that the $p$-$n$ depletion region becomes thin enough to permit Ohmic contact to the crystal interior (likely via tunneling) [10,40], the low-resistance metallic $n$-type bulk then dominating the $p$-type surface layer.

Figures 1(b) and 1(c) thus demonstrate that at moderate doping, on the insulating side of the IMT, i.e., in the range of interest for photovoltaics, the internal $p$-$n$ junction in pyrite single crystals can be effectively mitigated with *ex situ* sulfidized $CoS_2$ contacts, providing direct access to bulk transport properties. In terms of establishing the *mechanism* of this mitigation, we first note, as described in the Supplemental Material, Sec. B (Fig. S1) [29], that subjecting $FeS_2$ crystals to the same S atmosphere thermal treatment *before* contact deposition does *not* lead to junction mitigation, highlighting the importance of thermal treatment of the Co/$FeS_2$ *interface*. Experiments were thus performed to verify $CoS_2$ formation and probe the depth profile of Co in the $FeS_2$ crystals after sulfidation [as depicted in Fig. 2(a)]. As shown in the inset to Fig. 2(b), the conditions employed for *ex situ* sulfidation of Co overlayers [20] indeed result in single-phase $CoS_2$ by XRD: the expected 200, 210, 211, and 220 reflections are observed, yielding a lattice parameter (5.54 Å) consistent with the literature [19,20,41]. As further confirmation, the inset to Fig. 2(c) shows $T$-dependent magnetization data on such films, indicating $T_C \approx 120$ K, consistent with $CoS_2$ [18–20].

TOF SIMS (see the Supplemental Material, Sec. C [29], for details, including Fig. S2) was then used to quantify Co depth profiles. Figures 2(b) and 2(c) show depth profiles ($\log_{10}$ scale) of the TOF SIMS intensity for $Co^-$ and $CoS_2^-$ secondary ions, respectively, for *ex situ* sulfidized $CoS_2$(120 nm)/$FeS_2$ contacts (maroon), and, for comparison, as-deposited Co(30 nm)/$FeS_2$ contacts (black). Examining the as-deposited Co/$FeS_2$ contacts first, as expected, we find a ~30 nm region above the interface (i.e., negative depth in Fig. 2) with high $Co^-$ and low $CoS_2^-$ intensity. As sputtering proceeds into the $FeS_2$, the $Co^-$ intensity drops ~$10^3$-fold within 100 nm [Fig. 2(b)], while the $CoS_2^-$ signal [Fig. 2(c)] first rises abruptly (illustrating the sharpness of the Co/$FeS_2$ interface), before falling two orders of magnitude in 100 nm, i.e., on the same approximate length scale as the $Co^-$ decay. Importantly, this establishes baseline behavior for the apparent Co depth profile in $FeS_2$ crystals due to TOF SIMS artifacts such as cascade mixing [42]. Moving to $CoS_2$ contacts, Figs. 2(b) and 2(c) first show the expected high $Co^-$ and $CoS_2^-$ intensities throughout the 120 nm thick $CoS_2$ film (i.e., at negative depth). More significantly, these intensities remain at or above this level to ~50 nm into the $FeS_2$. Both intensities then drop rapidly, with similar form to the as-deposited Co/$FeS_2$, but with a *distinct 30–50 nm shift to higher depths*. *Ex situ* sulfidation thus induces not only reaction of Co contacts to $CoS_2$ [Figs. 2(b) and 2(c), insets], but also clear $CoS_2$/$FeS_2$ interdiffusion [Figs. 2(a)–2(c)], generating

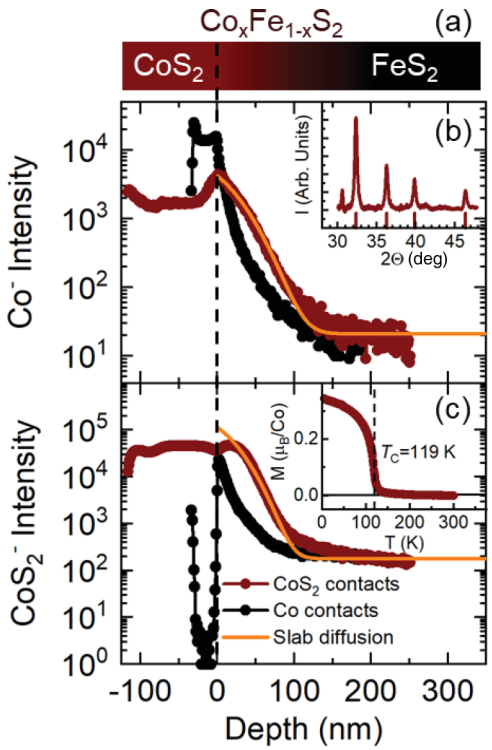


FIG. 2. (a) Schematic composition profile of a $CoS_2$-contacted $FeS_2$ crystal. Time of flight secondary ion mass spectrometry (TOF SIMS) depth profiles ($\log_{10}$ scale) of (b) $Co^-$ and (c) $CoS_2^-$ through the interface of an $FeS_2$ crystal contacted with ~120 nm of sulfidized $CoS_2$ (maroon); for reference, data for ~30 nm as-deposited Co contacts are also shown (black). Orange lines represent a 1D diffusion model with diffusivity $D \approx 2 \times 10^{-16}\,\mathrm{cm}^2\,\mathrm{s}^{-1}$ (see the Supplemental Material, Sec. D [29], for details). The insets to (b), (c) show an XRD pattern [intensity ($I$) vs $2\theta$] and magnetization ($M$) vs temperature ($T$) for representative 120–240 nm thick $CoS_2$ films. Expected $CoS_2$ reflections [19,20,41] are marked; the peak near 30.5° likely arises from the sample holder. $M(T)$ was measured in 500 Oe after field cooling in 500 Oe.

significant Co doping 30–50 nm into the $FeS_2$. In simple terms, a tens of nm deep Co-doped $n^+$ region is thus generated under the $CoS_2$, yielding direct Ohmic contact with the bulk, via the mechanisms elucidated below.

Further quantification is provided by the solid orange lines through the $CoS_2$-contacted data in Figs. 2(b) and 2(c), which are fits to a one-dimensional (1D) diffusion model, yielding a diffusion coefficient $D \approx 2 \times 10^{-16}\,\mathrm{cm}^2\,\mathrm{s}^{-1}$ (see the Supplemental Material, Sec. D [29], for details). $D(T)$ data for Co in $FeS_2$ are not available to our knowledge, but the similar ionic radii of $Co^{2+}$ and $Fe^{2+}$, and full solubility in $Fe_{1-x}Co_xS_2$ [19,41], suggest similarity to Fe self-diffusion in $FeS_2$. $D \approx 8 \times 10^{-16}\,\mathrm{cm}^2\,\mathrm{s}^{-1}$ at 350 °C for the latter [43], reassuringly close to our extracted value, verifying that the profiles in Fig. 2 are *quantitatively* consistent with expected diffusivities. As detailed in the Supplemental Material, Sec. D [29], an $n$-doping profile can then be constructed under simple assumptions, such as full dopant activation, accounting for detector saturation, and background effects. This is shown in Fig. S3 [29], indicating that doping as heavy as $n = 10^{20}\,\mathrm{cm}^{-3}$ is maintained at up to 100 nm depth under $CoS_2$ contacts.

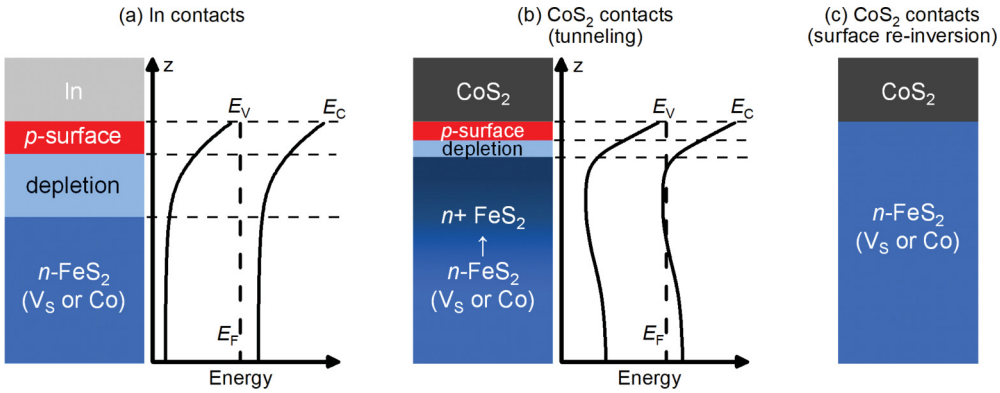


FIG. 3. Schematic illustrations and band diagrams directly under contacts formed with (a) conventional In and (b), (c) interdiffused $CoS_2$. The $n$-bulk, $p$-$n$ depletion regions, $p$-surface regions, and contact layers are shown, along with the conduction band ($E_C$), valence band ($E_V$), and Fermi ($E_F$) energies. The different scenarios in (b), (c) correspond to shrinking of the depletion region to the point of tunneling and direct (re)inversion of the $p$-surface layer, respectively, as discussed in the text.

Based on such information, Fig. 3 shows schematic illustrations of the situations realized directly under the contacts used here, thus elucidating the possible mechanisms for mitigation of the internal junction. Illustrated first in Fig. 3(a) is the situation with In contacts, showing the contact metal, heavily doped $p$-type surface layer, depletion region, $n$-type bulk, and resulting band bending [as in Fig. 1(a)]. One possibility for the situation under $CoS_2$ contacts is then illustrated in Fig. 3(b), which shows heavier doped ($n^+$) $FeS_2$ near the surface (due to in-diffusion of Co), thus shrinking the depletion region, narrowing the surface band bending region, and enabling tunneling from the $CoS_2$ metallic contact (and heavily doped $p$-surface layer) to the $n$-$FeS_2$ bulk. This is a known mechanism for Ohmic contacts to semiconductors [40]. Alternatively, and as illustrated in Fig. 3(c), the near-surface Co doping could be sufficiently heavy to (re)invert the $p$-surface, thereby realizing a direct $n$-$CoS_2$/$n$-$FeS_2$ interface and eliminating the internal $p$-$n$ junction under the contact.

We emphasize two further points about these mechanisms. First, the schematics in Figs. 3(b) and 3(c) represent the situation in the immediate vicinity of the $CoS_2$ contacts only; the remainder of the macroscopic crystal is unaffected, enabling characterization of bulk transport properties of unperturbed bulk $FeS_2$ crystals. Second, the internal $p$-$n$ junction mitigation demonstrated here is possible only due to (i) the metallic nature of $CoS_2$ [19,20]; (ii) the fact that Co is a shallow donor in $FeS_2$ [10,21–24]; and (iii) the significant diffusivity of Co in $FeS_2$ at moderate temperatures [43]. Simpler thermal treatments such as vacuum annealing of Co contacts could *not* achieve this, due to the decomposition of the $FeS_2$ surface to pyrrhotite $Fe_{1-x}S$, which commences at as low as ~160 °C [26].

With $CoS_2$ contact based mitigation of the internal $p$-$n$ junction in $FeS_2$ crystals demonstrated, low $T$ measurements of bulk transport properties of moderately doped semiconducting crystals become possible. We illustrate this in Fig. 4 by focusing on two representative crystals, one Co doped (red, left panels) and one $V_S$ doped (green, right panels), both with $n(300\,\mathrm{K}) \approx 1 \times 10^{17}\,\mathrm{cm}^{-3}$, i.e., in the doping range where low $T$ bulk transport is normally obfuscated by the internal junction [Figs. 1(b) and 1(c)]. Shown are the $T$ dependence ($\log_{10}$ scale) of $\rho$ [panels (a), (e)], $n$ [panels (b), (f)], the apparent Hall mobility $\mu$ [panels (c), (g)], and the 9 T perpendicular to plane magnetoresistance ($\mathrm{MR}(9\,\mathrm{T}) = [\rho(B)–\rho(0)]/\rho(0)$) [panels (d), (h)].

Focusing first on Co doping (left panels), Fig. 4(a) shows that $\rho(T)$ is metalliclike on cooling from 400 K but then increases significantly between ~100 and 1.8 K, indicating transport on the insulating side of the IMT. This is consistent with the doping progression in $CoS_2$-contacted crystals in Figs. 1(b)–1(d), and a thorough study of the IMT in $FeS_2$:Co [39], which places the critical electron density ($n_c$) at $\sim 2 \times 10^{17}\,\mathrm{cm}^{-3}$. Most noteworthy in Fig. 4(a) is the sharp slope discontinuity at ~20 K, marked with the dashed line. The origin of this is clarified by the Zabrodskii plot [44] in the inset. Such plots display $\ln W$ vs $\ln T$, where $W = -d(\ln \rho)/d(\ln T)$, in order to linearize $\rho = \rho_0 \exp(T_0/T)^m$, where $\rho_0 = \rho(T \to \infty)$, $T_0$ is a doping-dependent constant, and the exponent $m$ reveals the semiconducting transport mechanism [44]. As illustrated by the solid line in the inset, the ~20 K feature marks an abrupt crossover from a regime where $\ln W$ decreases on cooling to a regime with $m \approx \frac{1}{2}$, corresponding to ES VRH [25]. As also shown in the $\ln\rho$ vs $T^{-1/2}$ plot in the Supplemental Material, Sec. E, Fig. S4(a) [29], the $m \approx \frac{1}{2}$ regime spans ~20 to 1.8 K (i.e., an order of magnitude in $T$), and two orders of magnitude in $\rho$, thus establishing ES VRH with confidence. The extracted $T_0 = 65$ K is quite low [25], indicating relative proximity to the IMT, consistent with $n/n_c \approx 0.5$. The data of Fig. 4(a) thus indicate an abrupt $T$-dependent bulk crossover from diffusive to hopping transport at cryogenic temperatures. This demonstrates that state of the art pyrite single crystals exhibit bulk behavior strikingly reminiscent of prototypical doped semiconductors such as Ge [25,45].

As seen in Fig. 4(b), the diffusive to hopping crossover is yet more conspicuous in $n(T)$. As illustrated by the solid line fit and Arrhenius plot in the Supplemental Material, Sec. F [Fig. S5(a)] [29], activated behavior occurs above ~20 K, with an activation energy $\Delta E = 4.9$ meV. Importantly, due to the prior inability to probe bulk transport below ~100–200 K, and the low $\Delta E$ for Co, it is difficult to find literature values for comparison. Comparison to donor ionization energies from the hydrogenic model is possible,

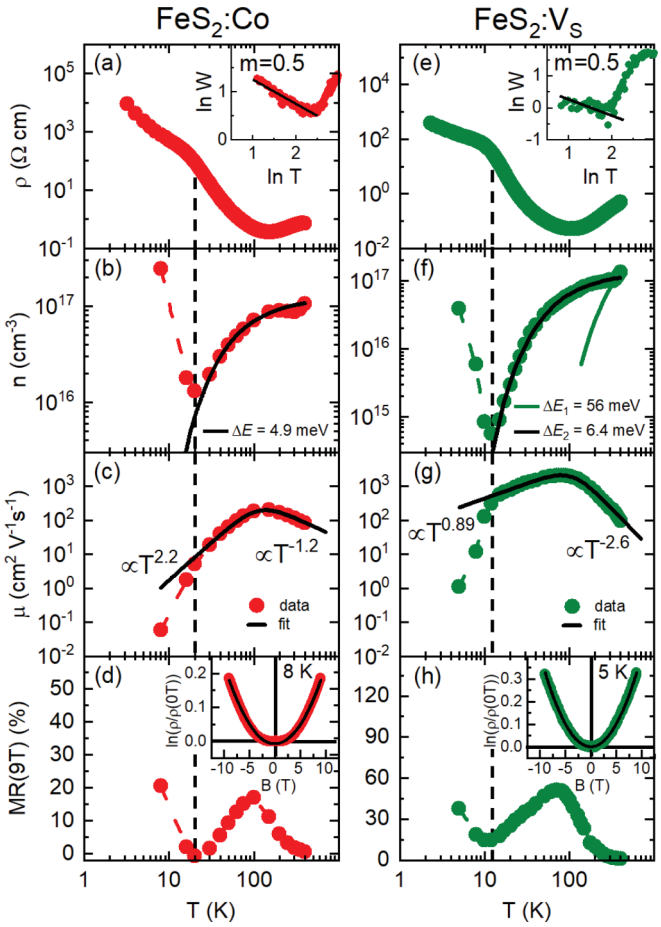


FIG. 4. Electronic transport data on $CoS_2$-contacted $FeS_2$ crystals doped to room temperature Hall electron densities [$n(300\,\mathrm{K})$] $\approx 1 \times 10^{17}\,\mathrm{cm}^{-3}$ with Co [(a)–(d), red] and $V_S$ [(e)–(h), green]. [The $V_S$-doped crystal is from Fig. 1(b)]. Shown are the temperature ($T$) dependence ($\log_{10}$ scale) of (a), (e) the resistivity ($\rho$), (b), (f) the low magnetic field Hall electron density ($n$), (c), (g) the resulting Hall mobility ($\mu$), and (d), (h) the 9 T perpendicular to plane magnetoresistance, $\mathrm{MR}(9\,\mathrm{T}) = [\rho(B)–\rho(0)]/\rho(0)$. The Arrhenius fits to $n(T)$ in (b),(f) yield the shown activation energies ($\Delta E$). The power law fits to $\mu(T)$ in (c), (g) yield the shown exponents. The insets in (a), (e) are Zabrodskii plots [$\ln W$ vs $\ln T$, where $W = -d(\ln R)/d(\ln T)$], linearizing $\rho = \rho_0 \exp(T_0/T)^m$ and yielding the exponent $m$ from the slope; the black lines correspond to $m = \frac{1}{2}$, i.e., Efros-Shklovskii variable-range hopping (ES VRH). The insets to (d), (h) show the magnetic field ($B$) dependence of $\ln[\rho(B)/\rho(0)]$ for Co- and $V_S$-doped crystals at 8 and 5 K, respectively; the black lines are fits to an ES VRH model yielding localization lengths ($L_c$) of 13 and 16 nm, respectively. Colored dashed lines connect the points, and vertical black dashed lines mark the diffusive-hopping crossovers.

however. While uncertainties exist with respect to the effective mass and dielectric constant in $FeS_2$, the best available values of $m_e^* \approx 0.5 m_e$ [17,46,47] and $\varepsilon_r \approx 20$ [48] yield a ∼16 meV donor ionization energy. This is not inconsistent with our observation, the measured $\Delta E = 4.9$ meV potentially being decreased from the ∼16 meV noninteracting donor ionization energy due to approach to the IMT ($n/n_c \approx 0.5$ here) [25,45]. We note as an aside that such values are distinctly lower than the 90 meV inferred from optical absorption [24], highlighting the importance of bulk transport characterization. Returning to Fig. 4(b), as $T$ is lowered from the diffusive to hopping regime, below ∼20 K, a dramatic *apparent* increase in $n$ occurs. This reflects the well-known suppression of the Hall coefficient in hopping transport [27,49–52], however, Fig. 4(b) thus being qualitatively consistent with Fig. 4(a). As expected, based on the above, there is no evidence of an $n$-type bulk to $p$-type surface crossover (as with conventional contacts) but rather a bulk $n$-type diffusive to hopping crossover.

Figure 4(c) shows the resulting Hall mobility, $\mu$. Classic moderately doped semiconducting behavior occurs, $\mu$ first increasing on cooling in a phonon scattering limited regime, before decreasing in an ionized impurity limited regime [40]. A peak mobility of $200\,\mathrm{cm}^2\,\mathrm{V}^{-1}\,\mathrm{s}^{-1}$ is attained at 150 K. The solid line in Fig. 4(c) is a fit to a simplified model describing both regimes with power laws and using Matthiessen's rule (additive scattering rates) to write $[\mu(T)]^{-1} = (aT^{-\alpha})^{-1} + (bT^{\beta})^{-1}$, where $\alpha$ and $\beta$ describe phonon and ionized impurity scattering, respectively ($a$ and $b$ are constants) [40]. A good fit is obtained over the entire diffusive transport regime ($20 < T < 400\,\mathrm{K}$), yielding reasonable values of $\alpha = 1.2$ and $\beta = 2.2$. More significantly, at ∼20 K, the apparent mobility begins to abruptly drop (due to the apparent rise in $n$ from Hall coefficient suppression), right at $\mu \approx 1\,\mathrm{cm}^2\,\mathrm{V}^{-1}\,\mathrm{s}^{-1}$. The bulk hopping to diffusive crossover thus occurs very close to the generic $\sim 1\,\mathrm{cm}^2\,\mathrm{V}^{-1}\,\mathrm{s}^{-1}$ often touted as an approximate threshold for diffusive band transport [27,53,54].

Figure 4(d) then shows the $T$-dependent MR ratio in a 9 T perpendicular field. At $T > 20\,\mathrm{K}$, classic ordinary MR is observed, with positive sign, parabolic $B$ dependence, and MR($T$) [Fig. 4(d)] that tracks $\mu(T)$ [Fig. 4(c)] (see the Supplemental Material, Sec. G, Figs. S6 and S7 [29], for details). Below 20 K, the positive MR then abruptly increases. As shown in the inset to Fig. 4(d), $\ln[\rho(B)/\rho(0)]$ at these lowest $T$ exhibits parabolic $B$ dependence (solid line fit), characteristic of the field-induced wave-function overlap decrease in ES VRH [25]. The localization length $L_c$ can then be extracted using $\ln[\frac{\rho(B)}{\rho(0)}] = \frac{s}{\hbar^2} L_c^4 B^2 (\frac{T_0}{T})^{3/2}$ [25], where $s$ is a dimensionless constant (0.0015), $\hbar$ is the reduced Planck constant, and $T_0 = 65\,\mathrm{K}$ is known from $\rho(T)$ (Figs. 4(a) and S4(a) [29]). This yields $L_c = 13$ nm, expanded significantly over the hydrogenic Bohr radius (∼2.5 nm, subject to the same uncertainties as the donor ionization energy), again consistent with approaching the IMT ($n/n_c \approx 0.5$) [25,45]. Figure 4(d) thus establishes MR quantitatively consistent with a bulk diffusive to hopping crossover at ∼20 K, in accord with $\rho(T)$, $n(T)$, and $\mu(T)$ [Figs. 4(a)–4(c)].

Moving to $V_S$ doping (green, right panels), Fig. 4(e) reveals a similar situation to Fig. 4(a) but with slightly lower $\rho$ at low $T$ and a slightly lower crossover temperature of ∼12 K (vertical dashed line). Consequently, ES VRH is more difficult to establish definitively, but $m = 0.5$ does describe the low $T$ data in the inset to Fig. 4(e), consistent with $\ln\rho$ vs $T^{-1/2}$ (Supplemental Material Sec. E, Fig. S4(b) [29]). A low $T_0$ of ∼35 K is thus determined, indicating closer proximity to the IMT than the Co-doped sample, likely due to slightly higher doping. Significantly, $CoS_2$ contacts now enable us to fully explore the bulk $n(T)$ [Fig. 4(f)], for which prior work (which was limited to higher $T$ by the internal $p$-$n$ junction)

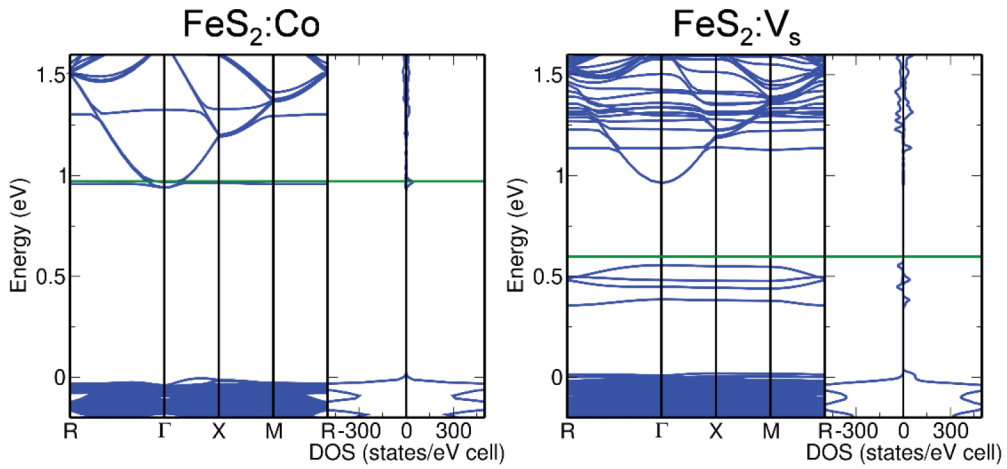


FIG. 5. Calculated band structure (left panels) and spin-polarized density of states (DOS, right panels) for (a) Co- and (b) $V_S$-doped pyrite. The green horizontal line marks the Fermi energy, the zero of energy is at the valence band maximum, and the DOS is shown for the two spin states. As described in the main text and in the Supplemental Material, Sec. H [29], these calculations involve $3 \times 3 \times 3$ supercells containing one $Co_{Fe}$ defect [in (a)] and a tetra-S-vacancy [in (b)]. In all cases, a Hubbard $U = 1.8$ eV was used on Fe, as optimized in prior work [17]. For the Co in (a), as discussed in the Supplemental Material [29], the $U = 3$ eV result is shown.

hinted at the possibility of two distinct activation energies in $FeS_2$:$V_S$ [10,16]. As illustrated by the solid line fits in Fig. 4(f) and the Arrhenius plots in Fig. S5(b) [29], two activated regimes indeed occur. At the highest $T$ (>325 K), $\Delta E_1 = 56$ meV, while $\Delta E_2 = 6.4$ meV describes the 12 K < $T$ < 325 K data. $\Delta E_1$ is consistent with earlier high $T$ measurements of $V_S$-doped $FeS_2$ crystals, which revealed a $\Delta E$ that gradually drops from the ~225 meV limiting value at light doping (the deep donor ionization energy) to ~17 meV at the heaviest $V_S$ doping achieved [10,16]. As already noted [16], this approach to the IMT due to doping with such a deep donor is very different from the better-understood approach to the IMT with shallow donors and can now be studied to low $T$ in $V_S$-doped pyrite. Although multiple activation energies and levels in the gap are known in certain semiconductors [40], the specific origin of the two distinct $\Delta E$ values here is unclear. In this regard, note that (i) we do not believe that $\Delta E_2$ is simply related to background Co impurities in $V_S$-doped crystals [16] as $\Delta E_2$ is not observed at all $V_S$ doping levels; (ii) just like $\Delta E_1$, $\Delta E_2$ collapses on approaching the IMT, from ~25 meV at $n(300\,\mathrm{K}) = 8 \times 10^{16}\,\mathrm{cm}^{-3}$ [10] to 6.4 meV at $n(300\,\mathrm{K}) \approx 1 \times 10^{17}\,\mathrm{cm}^{-3}$; (iii) in light of recent theoretical work [17], it is plausible that distinct types of $V_S$ clusters and/or $V_S$ interactions could produce multiple $\Delta E$. Further work will be required to resolve this, enabled by the internal junction mitigation demonstrated here. Regardless, cooling below ~12 K in Fig. 4(f) induces the same type of rapid increase in apparent $n$ as in Fig. 4(b), again reflecting the suppression of the Hall coefficient in the hopping regime [27,49–52].

Turning to mobility in the $V_S$-doped case, Fig. 4(g) again reveals a peak at intermediate $T$, this time reaching $2100\,\mathrm{cm}^2\,\mathrm{V}^{-1}\,\mathrm{s}^{-1}$ at 75 K. Significantly, this can be compared to peak mobilities of $2000\,\mathrm{cm}^2\,\mathrm{V}^{-1}\,\mathrm{s}^{-1}$ in Schieck *et al.* [55], $1930\,\mathrm{cm}^2\,\mathrm{V}^{-1}\,\mathrm{s}^{-1}$ in Limpinsel *et al.* [9], and ~$800\,\mathrm{cm}^2\,\mathrm{V}^{-1}\,\mathrm{s}^{-1}$ in Tomm *et al.* [56], demonstrating outstanding mobility. $\mu(T)$ is again described by $[\mu(T)]^{-1} = (aT^{-\alpha})^{-1} + (bT^{\beta})^{-1}$ across the entire diffusive regime (12–400 K), yielding $\alpha = 2.6$ and $\beta = 0.89$. The broad range of phonon-limited transport here (75–400 K, enabled by the mitigation of the internal *p-n* junction) in fact allows for more accurate determination of $\alpha$ than the Co-doped case, $\alpha = 2.6$ being in good agreement with several higher-$T$ $FeS_2$ studies [9,11,56]. Analogous to Co doping, and in accord with Figs. 4(e) and 4(f), the apparent $\mu(T)$ then abruptly drops at the ~12 K crossover to hopping transport.

The higher mobility in $V_S$-doped crystals, which we observe over the entire doping range, is particularly noteworthy. This amounts to as much as a factor of 10 in peak mobility between $V_S$ and Co doping in Figs. 4(c) and 4(g) ($2100\,\mathrm{cm}^2\,\mathrm{V}^{-1}\,\mathrm{s}^{-1}$; cf. $200\,\mathrm{cm}^2\,\mathrm{V}^{-1}\,\mathrm{s}^{-1}$), surely related to the rather different nature of the dopants. This is illustrated in Figs. 5(a) and 5(b), where DFT band structures and spin-resolved densities of states (DOS) are compared for Co- and $V_S$-doped pyrite. These figures show the expected ~0.95 eV band gap, the conduction band minimum being dominated by dispersive S 3 $p$ states [17]. As shown in Fig. 5(a), Co doping introduces a narrow band of defect states close to the conduction band minimum [57,58] (at ~0.95 eV in the left panel), corresponding to the small (spin-split) DOS peak in the right panel. As would be expected, the Fermi energy (green line) is then very close to the conduction band minimum. It should be noted, as discussed in the Supplemental Material, Sec. H (including Figs. S8 and S9) [29], that such results depend on the value of $U$ for Co. Low $U$ on Co (e.g., 2 eV) results in delocalized electrons populating the S 3 $p$ conduction band, high $U$ on Co (e.g., 4 eV) results in a localized donor state ~100 meV below the conduction band minimum, and $U = 3$ eV [as in Fig. 5(a)] results in a shallow donor state. The latter is clearly most consistent with experiment, and we thus focus on this case. Notably different is the $V_S$-doped case [Fig. 5(b)], which, based on prior work [17], was modeled with a tetra-S-vacancy generating a deep donor state. As shown in Fig. 5(b), the Fermi energy thus lies in the gap in these $3 \times 3 \times 3$ supercell calculations, the S 3 $p$ dominated conduction band being essentially unaffected. Comparison of Figs. 5(a) and

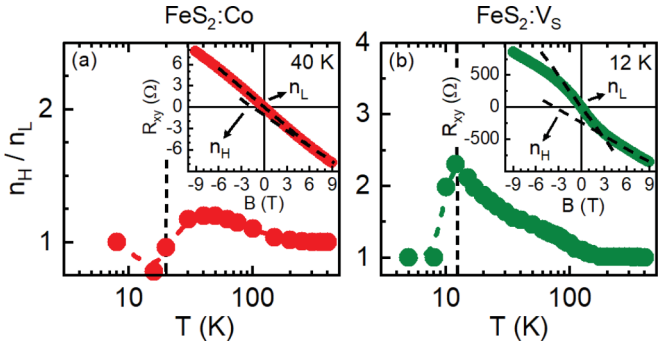


FIG. 6. Ratio of the Hall electron densities ($n_H/n_L$) extracted at high ($|B| \geqslant 7$ T) and low ($|B| \leqslant 1$ T) magnetic fields in the (a) Co-doped and (b) $V_S$-doped $FeS_2$ crystals in Fig. 4. The insets show transverse (Hall) resistance ($R_{xy}$) vs $B$ at 40 and 12 K for the Co- and $V_S$-doped crystals, respectively [i.e., the temperatures at which the nonlinearity in $R_{xy}(B)$ is maximum].

5(b) then provides a simple potential qualitative explanation for the higher electron mobilities in semiconducting $V_S$-doped $FeS_2$ compared to Co-doped $FeS_2$. The former has essentially unperturbed dispersive S 3 $p$ states in the conduction band, while Co doping generates a narrow band of states very close to the conduction band minimum, likely negatively impacting both $m_e^*$ and the electron-phonon scattering rate (through the increased DOS). Local magnetic moments on the Co dopants could yield yet more scattering, further decreasing the mobility.

Returning to Fig. 4 to complete the discussion of $FeS_2$:$V_S$ transport, Fig. 4(h) shows that the MR in $V_S$-doped crystals is similar to $FeS_2$:Co, again exhibiting the prototypical crossover from positive, parabolic, mobility-tracking ordinary MR in the diffusive regime (>12 K) to ES VRH MR at <12 K. The fit in the inset to Fig. 4(h) yields $L_c = 16$ nm, slightly larger than the 13 nm from Fig. 4(d), consistent with the lower $T_0$. Interestingly, as shown in the Supplemental Material, Sec. G [29], some evidence of subparabolic $B$ dependence emerges at intermediate $T$ (e.g., 75 K, Fig. S6(d) [29]). As will be discussed elsewhere [39], a significant regime of near $B$ linear positive MR can also be found in certain $T$ and doping regimes in Co-doped $FeS_2$ crystals, another unexpected finding enabled by access to low $T$ bulk transport.

As a final point, we emphasize that the results in Figs. 4(b), 4(c), 4(f), and 4(g) are based on low $|B|$ (<1 T) Hall measurements. At higher $|B|$, an interesting nonlinear Hall effect emerges, as shown in Fig. 6. The insets to Figs. 6(a) and 6(b) illustrate this effect in Co- and $V_S$-doped crystals, showing that the transverse (Hall) resistance ($R_{xy}$) is nonlinear in $B$. $dR_{xy}/dB$ evolves from a maximum at low $|B|$ to a smaller value at high $|B|$, which we simply quantify by extracting two apparent Hall densities, $n_L$ (at $|B| \leqslant 1$ T) and $n_H$ (at $|B| \geqslant 7$ T), as illustrated in the insets (dashed black lines). The ratio $n_H/n_L$ is then plotted vs $T$ in Figs. 6(a) and 6(b), revealing gradual rises in nonlinearity (i.e., $n_H/n_L > 1$) on cooling below ~200 K, maxima close to the crossovers to hopping (~20 and ~12 K for Co and $V_S$ doping), then rapid decreases as the Hall coefficient is suppressed in the hopping regime. Notably, the peak $n_H/n_L$ is around twice as large for the higher-mobility $V_S$-doped case than the Co-doped case. Generally, such Hall nonlinearity reflects multiple carrier populations, such as electrons and holes [59–61], multiple bands [62–64], bulk and surface channels [9,11,60,61,65] (as in lightly doped $FeS_2$ [9,11]), etc. We have definitively established bulk transport here, however, and the nonlinear Hall effect accompanying the $n$-type bulk to $p$-type surface crossover in conventionally contacted $FeS_2$ crystals is very different from Fig. 6. The only obvious possibilities for distinct transport contributions are thus from diffusive and hopping channels (due to inhomogeneity on the approach to the IMT, for example) or distinct donor states or donor bands in the gap, as discussed above in light of two activation energies and different mobilities in the $V_S$- and Co-doped cases. Further analysis along these lines is hindered by the absence of a theory of the Hall effect for coexisting diffusive and hopping channels, and uncertainties regarding the origin of the multiple activation energies. Further work will be required to clarify this, enabled by the access to low $T$ bulk transport properties provided by the internal junction mitigation demonstrated here. The observations in Fig. 6 are in fact a clear illustration of the many transport phenomena in doped $FeS_2$ previously obfuscated by the internal junction.

## IV. SUMMARY AND DISCUSSION

In summary, careful $T$-dependent transport measurements and analyses have been coupled with XRD and magnetometry characterization, and TOF SIMS depth profiling, to establish complete mitigation of the internal $p$-$n$ junction in $CoS_2$-contacted $FeS_2$ single crystals. The metallicity of $CoS_2$ [18,19], shallow donor nature of Co [10,21–24,66], and significant diffusivity of Co in $FeS_2$ [43] are simultaneously exploited to produce metallic $CoS_2$ contacts that also induce heavy diffusion doping of $FeS_2$ to tens of nm depths, generating direct Ohmic contact to the crystal interior [via mechanisms we have discussed (Fig. 3)]. This enables *bulk* transport studies of moderately doped semiconducting $FeS_2$, elucidating activation energies, multiple regimes of activated transport, electron mobilities up to 2100 $cm^2\,V^{-1}\,s^{-1}$, very different mobilities in Co- and $V_S$-doped cases, an abrupt $T$-dependent crossover from diffusive to hopping transport (strikingly reminiscent of prototypical doped semiconductors), and an unusual nonlinear Hall effect near the diffusive to hopping crossover. Such diffused $CoS_2$ contacts can now be tactically employed in future work, both for fundamental studies and for further development of pyrite-based photovoltaics.

In terms of implications of our findings from fundamental and applied (e.g., photovoltaic) perspectives, we wish to emphasize some key points. In terms of fundamental knowledge, the access to low $T$ bulk transport measurements provided here already elucidates very different donor level positions in Co- and $V_S$-doped cases, highlighting that further work is required to understand the two activation energies in $V_S$-doped $FeS_2$ and that Co indeed appears to be an ideal shallow donor. The order of magnitude lower peak mobility for Co doping (which we explain via the calculations presented in Fig. 5) was not anticipated, however, highlighting the desirability of doping beyond the IMT with $V_S$. In particular, the high mobilities in that case could enable quantum transport measurements

(e.g., of Shubnikov–de Haas oscillations), providing valuable fundamental information, including more accurate $m_e^*$ values; uncertainties due to the latter were noted several times above. Our findings also illustrate that further magnetotransport studies should be performed on $FeS_2$ crystals, exploring both the near $B$ linear MR (which is of high general interest [67]) and the nonlinear Hall effect shown in Fig. 6. More generally, the results of Fig. 4 establish that state of the art doped-$FeS_2$ single crystals are of sufficient electronic quality to enable detailed studies of both diffusive to hopping and insulator to metal transitions.

In terms of implications of our work for *applications* of pyrite, particularly in photovoltaic devices, we first note that Ohmic $CoS_2$-based contacts of the type established here are of clear utility for back contacts in solar cells. Back $CoS_2$ contacts paired with conventional top contacts could also enable *vertical* transport based characterization of the internal *p-n* junction in pyrite crystals (a significant step beyond prior work [10]), including voltage-dependent characterization. The latter would constitute a first step to potentially understanding and harnessing the naturally formed internal $FeS_2$ *p-n* junction for photovoltaic purposes. Wide $T$ range measurements of Hall electron and hole densities could also now enable further understanding of donor and acceptor levels. The results here already demonstrate how different these are for Co and $V_S$ donors and open up the determination of equivalent energies for potential acceptors. The latter are poorly established in pyrite, even though *p-n* homojunction devices offer a novel route to pyrite solar cells, potentially sidestepping issues with surface states. It has also been noted [7,9] that the deep donor nature of $V_S$ in pyrite could limit $V_{OC}$ in heterojunction devices, related to the band bending shown in Figs. 1(a) and 3. The current work establishes a means to assess $n(T)$ over a broad $T$ range in $FeS_2$ single crystals, thus reliably determining $V_S$-related donor levels, a prerequisite for controlling either the concentration or donor level position of $V_S$ in $FeS_2$.

## ACKNOWLEDGMENTS

This work was supported by the customers of Xcel Energy through the Renewables Development Fund, and in part by the National Science Foundation NSF through the University of Minnesota (UMN) MRSEC under Grant No. DMR-2011401. Work on Co-doped $FeS_2$ specifically was supported by the U.S. Department of Energy through the UMN Center for Quantum Materials under Grant No. DE-SC-0016371. Parts of this work were carried out in the Characterization Facility, UMN, which receives partial support from NSF through the MRSEC program. B.V. acknowledges the UMN Doctoral Dissertation Fellowship and D.R. acknowledges the Minnesota Supercomputing Institute for computing resources. We thank B. Shklovskii and T. Birol for informative discussions, and J. Batley for Co contact evaporation and discussions.

[1] C. Wadia, A. P. Alivisatos, and D. M. Kammen, Materials availability expands the opportunity for large-scale photovoltaics deployment, Environ. Sci. Technol. **43**, 2072 (2009).

[2] A. Ennaoui, S. Fiechter, C. Pettenkofer, N. Alonso-Vante, K. Büker, M. Bronold, C. Höpfner, and H. Tributsch, Iron disulfide for solar energy conversion, Sol. Energy Mater. Sol. Cells **29**, 289 (1993).

[3] A. Ennaoui and H. Tributsch, Iron sulphide solar cells, Sol. Cells **13**, 197 (1984).

[4] A. Ennaoui and H. Tributsch, Energetic characterization of the photoactive $FeS_2$ (pyrite) interface, Sol. Energy Mater. **14**, 461 (1986).

[5] A. Ennaoui, S. Fiechter, W. Jaegermann, and H. Tributsch, Photoelectrochemistry of highly quantum efficient single-crystalline $n$-$FeS_2$ (pyrite), J. Electrochem. Soc. **133**, 97 (1986).

[6] K. Büker, N. Alonso-Vante, and H. Tributsch, Photovoltaic output limitation of $n$-$FeS_2$ (pyrite) Schottky barriers: A temperature-dependent characterization, J. Appl. Phys. **72**, 5721 (1992).

[7] M. Cabán-Acevedo, N. S. Kaiser, C. R. English, D. Liang, B. J. Thompson, H. Chen, K. J. Czech, J. C. Wright, R. J. Hamers, and S. Jin, Ionization of high-density deep donor defect states explains the low photovoltage of iron pyrite single crystals, J. Am. Chem. Soc. **136**, 17163 (2014).

[8] D. Liang, M. Cabán-Acevedo, N. S. Kaiser, and S. Jin, Gated Hall effect of nanoplate devices reveals surface-state-induced surface inversion in iron pyrite semiconductor, Nano Lett. **14**, 6754 (2014).

[9] M. Limpinsel, N. Farhi, N. Berry, J. Lindemuth, C. L. Perkins, Q. Lin, and M. Law, An inversion layer at the surface of $n$-type iron pyrite, Energy Environ. Sci. **7**, 1974 (2014).

[10] B. Voigt, W. Moore, M. Maiti, J. Walter, B. Das, M. Manno, C. Leighton, and E. S. Aydil, Observation of an internal $p-n$ junction in pyrite $FeS_2$ single crystals: Potential origin of the low open circuit voltage in pyrite solar cells, ACS Mater. Lett. **2**, 861 (2020).

[11] J. Walter, X. Zhang, B. Voigt, R. Hool, M. Manno, F. Mork, E. S. Aydil, and C. Leighton, Surface conduction in $n$-type pyrite $FeS_2$ single crystals, Phys. Rev. Materials **1**, 065403 (2017).

[12] M. Bronold, K. Buker, S. Kubala, C. Pettenkofer, and H. Tributsch, Surface preparation of $FeS_2$ via electrochemical etching and interface formation with metals, Phys. Status Solidi **135**, 231 (1993).

[13] M. Bronold, Y. Tomm, and W. Jaegermann, Surface states on cubic $d$-band semiconductor pyrite ($FeS_2$), Surf. Sci. **314**, L931 (1994).

[14] R. Murphy and D. R. Strongin, Surface reactivity of pyrite and related sulfides, Surf. Sci. Rep. **64**, 1 (2009).

[15] F. W. Herbert, A. Krishnamoorthy, W. Ma, K. J. Van Vliet, and B. Yildiz, Dynamics of point defect formation, clustering and pit initiation on the pyrite surface, Electrochim. Acta **127**, 416 (2014).

[16] B. Voigt, W. Moore, M. Manno, J. Walter, J. D. Jeremiason, E. S. Aydil, and C. Leighton, Transport evidence for sulfur vacancies as the origin of unintentional $n$-type doping in pyrite $FeS_2$, ACS Appl. Mater. Interfaces **11**, 15552 (2019).

[17] D. Ray, B. Voigt, M. Manno, C. Leighton, E. S. Aydil, and L. Gagliardi, Sulfur vacancy clustering and its impact on electronic properties in pyrite $FeS_2$, Chem. Mater. **32**, 4820 (2020).

[18] H. Hiraka and Y. Endoh, Ferromagnetic transition of Heisenberg ferromagnetic metal of $CoS_2$—Static critical properties, J. Phys. Soc. Jpn. **63**, 4573 (1994).

[19] C. Leighton, M. Manno, A. Cady, J. W. Freeland, L. Wang, K. Umemoto, R. M. Wentzcovitch, T. Y. Chen, C. L. Chien, P. L. Kuhns, M. J. R. Hoch, A. P. Reyes, W. G. Moulton, E. D. Dahlberg, J. Checkelsky, and J. Eckert, Composition controlled spin polarization in $Co_{1-x}Fe_xS_2$ alloys, J. Phys.: Condens. Matter **19**, 315219 (2007).

[20] M. Manno, R. Frakie, and C. Leighton, Synthesis and characterization of highly spin-polarized single-phase $Co_{1-x}Fe_xS_2$ films, J. Appl. Phys. **105**, 093912 (2009).

[21] S. W. Lehner, K. S. Savage, and J. C. Ayers, Vapor growth and characterization of pyrite ($FeS_2$) doped with Co, Ni, and As: Variations in semiconducting properties, J. Cryst. Growth **286**, 306 (2006).

[22] S. Guo, D. P. Young, R. T. Macaluso, D. A. Browne, N. L. Henderson, J. Y. Chan, L. L. Henry, and J. F. Ditusa, Discovery of the Griffiths Phase in the Itinerant Magnetic Semiconductor $Fe_{1-x}Co_xS_2$, Phys. Rev. Lett. **100**, 017209 (2008).

[23] S. Guo, D. P. Young, R. T. Macaluso, D. A. Browne, N. L. Henderson, J. Y. Chan, L. L. Henry, and J. F. Ditusa, Charge transport in cobalt-doped iron pyrite, Phys. Rev. B **81**, 144424 (2010).

[24] S. W. Lehner, N. Newman, M. Van Schilfgaarde, S. Bandyopadhyay, K. Savage, and P. R. Buseck, Defect energy levels and electronic behavior of Ni-, Co-, and As-doped synthetic pyrite ($FeS_2$), J. Appl. Phys. **111**, 083717 (2012).

[25] B. I. Shklovskii and A. L. Efros, *Electronic Properties of Doped Semiconductors* (Springer, Berlin, 1984).

[26] X. Zhang, T. Scott, T. Socha, D. Nielsen, M. Manno, M. Johnson, Y. Yan, Y. Losovyj, P. Dowben, E. S. Aydil, and C. Leighton, Phase stability and stoichiometry in thin film iron pyrite: Impact on electronic transport properties, ACS Appl. Mater. Interfaces **7**, 14130 (2015).

[27] X. Zhang, M. Li, J. Walter, L. O'Brien, M. A. Manno, B. Voigt, F. Mork, S. V. Baryshev, J. Kakalios, E. S. Aydil, and C. Leighton, Potential resolution to the doping puzzle in iron pyrite: Carrier type determination by Hall effect and thermopower, Phys. Rev. Materials **1**, 015402 (2017).

[28] J. Walter, B. Voigt, E. Day-Roberts, K. Heltemes, R. M. Fernandes, T. Birol, and C. Leighton, Voltage-induced ferromagnetism in a diamagnet, Sci. Adv. **6**, eabb7721 (2020).

[29] See Supplemental Material at http://link.aps.org/supplemental/10.1103/PhysRevMaterials.5.025405 for additional information on crystal growth, transport measurement methods, TOF-SIMS data acquisition and analysis, interdiffusion quantification, variable-range hopping analysis, Arrhenius analysis, magnetotransport data and analysis, and DFT calculations.

[30] G. Kresse and J. Hafner, *Ab initio* molecular dynamics for liquid metals, Phys. Rev. B **47**, 558 (1993).

[31] G. Kresse and J. Hafner, *Ab initio* molecular-dynamics simulation of the liquid-metal–amorphous-semiconductor transition in germanium, Phys. Rev. B **49**, 14251 (1994).

[32] G. Kresse and J. Furthmüller, Efficient iterative schemes for *ab initio* total-energy calculations using a plane-wave basis set, Phys. Rev. B **54**, 11169 (1996).

[33] G. Kresse and J. Furthmüller, Efficiency of *ab-initio* total energy calculations for metals and semiconductors using a plane-wave basis set, Comput. Mater. Sci. **6**, 15 (1996).

[34] P. E. Blöchl, Projector augmented-wave method, Phys. Rev. B **50**, 17953 (1994).

[35] G. Kresse, From ultrasoft pseudopotentials to the projector augmented-wave method, Phys. Rev. B **59**, 1758 (1999).

[36] J. P. Perdew and Y. Wang, Accurate and simple analytic representation of the electron-gas correlation energy, Phys. Rev. B **45**, 13244 (1992).

[37] J. P. Perdew, K. Burke, and M. Ernzerhof, Generalized Gradient Approximation Made Simple, Phys. Rev. Lett. **77**, 3865 (1996).

[38] A. Rohrbach, J. Hafner, and G. Kresse, Electronic correlation effects in transition-metal sulfides, J. Phys.: Condens. Matter **15**, 979 (2003).

[39] B. Das, B. Voigt, M. Maiti, M. Manno, E. S. Aydil, and C. Leighton, Insulator-metal transition in Co-doped pyrite single crystals (unpublished).

[40] S. M. Sze, *Physics of Semiconductor Devices* (John Wiley & Sons, New York, 1981).

[41] T. Kinner, K. P. Bhandari, E. Bastola, B. M. Monahan, N. O. Haugen, P. J. Roland, T. P. Bigioni, and R. J. Ellingson, Majority carrier type control of cobalt iron sulfide ($Co_xFe_{1-x}S_2$) pyrite nanocrystals, J. Phys. Chem. C **120**, 5706 (2016).

[42] P. Williams and J. E. Baker, Quantitative analysis of interfacial impurities using secondary-ion mass spectrometry, Appl. Phys. Lett. **36**, 842 (1980).

[43] J. H. Chen and W. W. Harvey, Cation self-diffusion in chalcopyrite and pyrite, Metall. Trans. B **6**, 331 (1975).

[44] A. G. Zabrodskii, The Coulomb gap: The view of an experimenter, Philos. Mag. B **81**, 1131 (2001).

[45] N. Mott, *Metal-Insulator Transitions*, 2nd ed. (Taylor & Francis, London, 1990).

[46] A. M. Karguppikar and A. G. Vedeshwar, Transport properties of thin iron pyrite films, Phys. Status Solidi **95**, 717 (1986).

[47] J. Hu, Y. Zhang, M. Law, and R. Wu, First-principles studies of the electronic properties of native and substitutional anionic defects in bulk iron pyrite, Phys. Rev. B **85**, 085203 (2012).

[48] S. G. Choi, J. Hu, L. S. Abdallah, M. Limpinsel, Y. N. Zhang, S. Zollner, R. Q. Wu, and M. Law, Pseudodielectric function and critical-point energies of iron pyrite, Phys. Rev. B **86**, 115207 (2012).

[49] L. Friedman, Hall conductivity of amorphous semiconductors in the random phase model, J. Non-Cryst. Solids **6**, 329 (1971).

[50] P. G. Le Comber, D. I. Jones, and W. E. Spear, Hall effect and impurity conduction in substitutionally doped amorphous silicon, Philos. Mag. A **35**, 1173 (1977).

[51] J. Kakalios, A physical interpretation of the Hall effect in amorphous semiconductors, J. Non-Cryst. Solids **114**, 372 (1989).

[52] Y. M. Gal'perin, E. P. German, and V. G. Karpov, Hall effect under hopping conditions, Zh. Eksp. Teor. Fiz. **99**, 343 (1991) [J. Exp. Theor. Phys. **72**, 193 (1991)].

[53] S. Stafström, Electron localization and the transition from adiabatic to nonadiabatic charge transport in organic conductors, Chem. Soc. Rev. **39**, 2484 (2010).

[54] S. Wang, M. Ha, M. Manno, C. D. Frisbie, and C. Leighton, Hopping transport and the Hall effect near the insulator-metal transition in electrochemically gated poly(3-hexylthiophene) transistors, Nat. Commun. **3**, 1210 (2012).

[55] R. Schieck, A. Hartmann, S. Fiechter, R. Könenkamp, and H. Wetzel, Electrical properties of natural and synthetic pyrite ($FeS_2$) crystals, J. Mater. Res. **5**, 1567 (1990).

[56] Y. Tomm, R. Schieck, K. Ellmer, and S. Fiechter, Growth mechanism and electronic properties of doped pyrite ($FeS_2$) crystals, J. Cryst. Growth **146**, 271 (1995).

[57] P. Lazi, R. Armiento, F. W. Herbert, R. Chakraborty, R. Sun, M. K. Y. Chan, K. Hartman, T. Buonassisi, B. Yildiz, and G. Ceder, Low intensity conduction states in $FeS_2$: Implications for absorption, open-circuit voltage and surface recombination, J. Phys.: Condens. Matter **25**, 465801 (2013).

[58] E. Day-Roberts, T. Birol, and R. M. Fernandes, Contrasting ferromagnetism in pyrite $FeS_2$ induced by chemical doping versus electrostatic gating, Phys. Rev. Materials **4**, 054405 (2020).

[59] N. P. Armitage, E. J. Mele, and A. Vishwanath, Weyl and Dirac semimetals in three-dimensional solids, Rev. Mod. Phys. **90**, 015001 (2018).

[60] M. Z. Hasan and C. L. Kane, Colloquium: Topological insulators, Rev. Mod. Phys. **82**, 3045 (2010).

[61] X. L. Qi and S. C. Zhang, Topological insulators and superconductors, Rev. Mod. Phys. **83**, 1057 (2011).

[62] H. Yang, Y. Liu, C. Zhuang, J. Shi, Y. Yao, S. Massidda, M. Monni, Y. Jia, X. Xi, Q. Li, Z. K. Liu, Q. Feng, and H. H. Wen, Fully Band-Resolved Scattering Rate in $MgB_2$ Revealed by the Nonlinear Hall Effect and Magnetoresistance Measurements, Phys. Rev. Lett. **101**, 067001 (2008).

[63] S. Stemmer and S. J. Allen, Two-dimensional electron gases at complex oxide interfaces, Annu. Rev. Mater. Res. **44**, 151 (2014).

[64] J. A. Sulpizio, S. Ilani, P. Irvin, and J. Levy, Nanoscale phenomena in oxide heterostructures, Annu. Rev. Mater. Res. **44**, 117 (2014).

[65] H. Wang, J. Walter, K. Ganguly, B. Yu, G. Yu, Z. Zhang, H. Zhou, H. Fu, M. Greven, and C. Leighton, Wide-voltage-window reversible control of electronic transport in electrolyte-gated epitaxial $BaSnO_3$, Phys. Rev. Materials **3**, 075001 (2019).

[66] R. N. Chandler and R. W. Bené, EPR study of the solid solutions $Ni_xFe_{1-x}S_2$, $Co_xFe_{1-x}S_2$, and $Co_xNi_yFe_{1-x-y}S_2$, Phys. Rev. B **8**, 4979 (1977).

[67] J. Singleton, Temperature scaling behavior of the linear magnetoresistance observed in high-temperature superconductors, Phys. Rev. Materials **4**, 061801(R) (2020).